J Mater Sci (2012) 47:23–40
DOI 10.1007/s10853-011-5897-6

ANNIVERSARY REVIEW

From micro to nanocrystalline diamond grown on 3D porous titanium matrix

N. A. Braga · M. R. Baldan · N. G. Ferreira

Received: 27 May 2011 / Accepted: 23 August 2011 / Published online: 9 September 2011

Abstract This study aims to give an overview on the growth process and characterization of electrodes produced by coating three-dimensional (3D) titanium (Ti) substrates with diamond films. Powder metallurgy (P/M) was the technique used to obtain the desired and controlled 3D porosity in the Ti matrix. As an important role, in the first place, the effect of a hydrogenation process on the 3D Ti substrate during the diamond growth is presented and discussed. In addition, a detailed description was done about the main growth parameters to obtain these 3D diamond electrodes in the micro and nano scale. The experimental parameters analyzed were the pressure inside the reactor, the methane and the argon gas concentrations, and the temperature at the substrate surface. Scanning electron microscopy, Grazing incident X-ray diffraction and Raman spectroscopy were the techniques used to characterize all the diamond films in the point of view of their morphology, structure, and sp^2/sp^3 ratio. Finally, the results concerning the electrochemical characterization of these 3D micro and nanocrystalline diamond electrodes are discussed.

Introduction

Titanium (Ti) is a metal that presents excellent physical and mechanical properties. The high tensile strength of about 435 MPa of this metal [1] associated with its low density (4.54 g cm^{-3}) confers to it the most important and desirable mechanical properties for structural applications, concerning its high strength-to-weight ratio. Among the Ti chemical properties, its high reactivity can be highlighted, which can be appointed as a disadvantage for the Ti processing [1, 2]. As a rule, pure Ti and its alloys present excellent corrosion resistance to seawater and chloride aqueous solutions, oxidative environment, dilute aqueous solutions of reducing agents as HCl and H_2SO_4, and organic acids.

Owing to the properties discussed above, Ti is expensive to produce, to manufacture, to machine, and especially difficult to obtain by processing through the liquid phase. Powder metallurgy (P/M) emerges as a technique where all these difficulties can be diluted, producing volumetric Ti at low temperatures and under conditions that allow the consolidation of the metal in the solid phase [3, 4]. This process also minimizes the problems associated with its high chemical reactivity. Besides, the costs can be reduced using techniques known as “near-net shape”, i.e., production of metal parts and/or their artifacts in the desired final form [5–11].

Despite its excellent mechanical properties, titanium has a low resistance to cyclic stress and erosion. Thus, in recent years, some works have demonstrated that the diamond film covering this metal is a way to promote a significant improvement in the Ti mechanical properties [12–19]. The diamond works as a coating, which is extremely hard, resistant to corrosion, thermal conductive, and low frictional on Ti substrate [20–28]. The most widespread technique for the growth of diamond films on titanium substrates is the Chemical vapor deposition (CVD). The CVD-diamond growth process consists in the formation of atomic hydrogen and hydrocarbon radicals (methyl or

---

N. A. Braga (✉)
Departamento de Química, Instituto de Ciências Exatas,
Universidade Federal do Amazonas, UFAM, Manaus,
Am 69077-000, Brazil
e-mail: neilabraga@ufam.edu.br

M. R. Baldan · N. G. Ferreira
Instituto Nacional de Pesquisas Espaciais, INPE,
São José dos Campos, SP 12245-970, Brazil

ethyl, for example) inside a reactor under no equilibrium thermodynamic conditions. Such reactive species can be produced in a high energy zone activated by hot filaments (hot filament chemical vapor deposition—HFCVD) or plasma source (Plasma-enhanced chemical vapor deposition (PECVD) [29–35]. The produced hydrocarbon and radical atoms are incorporated into the metal surface providing the growth of the diamond lattice [36–40].

The process to cover titanium substrates with a CVD-diamond film has its disadvantage attributed to the hydrogen diffused into the titanium matrix. This hydrogen diffusion promotes the formation of titanium hydride species, which in some cases may weaken the substrate. However, some studies show that the hydride generation can improve some mechanical properties [41, 42], for example, resistance to the cyclic stress, since the hydrides are responsible for the increase of the ductility in the metal matrix. Another important factor is that the hydride appears to improve the adhesion of the diamond film on the titanium substrate [43]. There are no studies which show or prove the role of substrate hydrogenation in the process of CVD-diamond deposition on porous titanium substrates.

The conditions and mechanisms of the diamond deposition on titanium substrates for these purposes represent a field of study only explored in the last decades, and therefore, not yet completely understood. Great attention has been given, in the literature, to the diamond growth on dense titanium substrates [43–50]. In an attempt to improve the film adhesion on such substrates, surface treatment techniques, such as ion implantations or bias effects on the diamond surface have been used [51, 52]. These techniques act by increasing the surface roughness and promoting the film anchoring.

A very little explored area is the deposition of diamond on titanium substrates containing high porosity, or even interconnected porosity. Such substrates can be obtained by powder metallurgy techniques, and their mechanical properties can be improved by this technique. The challenge refers to the Ti with high surface area and may provide more substrate hydrogenations. Consequently, a systematic study should be conducted in order to control the growth conditions to diminish the effects of hydrogenation and to understand the role of the titanium hydride in the mechanism of the CVD-diamond deposition process on porous Ti.

A real application of the materials obtained by coating porous titanium with CVD-diamond films is their use as electrode materials. By doping the deposited diamond film with some impurities like boron, nitrogen, or sulfur [53, 54] the diamond wide gap of 5.5 eV can be reduced, producing a semiconductor material [55]. This makes it possible to apply this material as a sensor, since the doping process reduces its resistivity. Doping with boron has achieved good results for applications such as sensors, both in solid-state electronics and semiconductors in electrochemical sensors [56]. The diamond film properties, such as high mobility of carriers, elevated thermal conductivity, electrical stability, and compatibility with aggressive media, can be widely explored in sensors for toxic gases and in electrodes for hostile chemical environments [57–61]. The decrease in resistivity of the diamond films is also achieved when they are grown at nanoscale. In this case, the large amount of sp^2 carbon bound at the grain boundaries of nanodiamond is responsible for the process of conducting material [23, 24, 44, 62, 63]. Nonetheless, there are few studies which underscore the growth and characterization of diamond electrodes deposited on titanium substrates and even fewer works dealing with electrodes containing three-dimensional porosity [23, 24, 44, 63]. These electrodes may combine the structural advantages of the metallic titanium with the relative advantages of the lightness of the structures containing porosity. These properties are combined with the excellent diamond structural properties and chemical stability.

Therefore, an overview of the growth process and characterization of the electrodes produced by coating 3D Ti substrates with diamond films by the CVD technique will be presented. First, the effect of the hydrogen gas on the morphology and structure of the Ti matrix and the consequence of the Ti hydrogenation for the obtained diamond films will be discussed. After that, the influence of the experimental parameters as pressure, temperature, gas composition on the quality, morphology, and structure of the diamond film grown on the 3D Ti substrates will also be discussed. Finally, the electrochemical characterization of the diamond/Ti electrodes will be dealt with.

Hydrogen effect on three-dimensional (3D) titanium matrix

In the 3D porosity, the surface and the bulk material are provided by planes, declivities, pores, walls or rods, so that a water drop can pass through the sample, which means that a water drop placed on the top surface of the sample will pass through its pores or channels and will reach the sample opposite side. So, the pores in the sample are open and interconnected, forming a pore net. It is important to point out that the pores or channels formed from the powder metallurgy process in these kinds of substrates are macrometric sized. Therefore, there are no limitations in the pore size related to the gas penetration during the diamond growth by the HFCVD process.

The P/M techniques can be used to prepare Ti substrates with desired 3D porosity from hydrogenated pure Ti powders by pre-form sintering processes. The details of this process as well as the morphologic characterization of the Ti substrates were recently published [64]. The hydride-dehydride (HDH) method was used to produce Ti powders with different particle sizes at 500 °C in a vertical furnace for 3 h under a pressure of 10^{-5} Pa [6]. After cooling, the Ti powders in the range of 250–350 µm were uniaxially pressed in an inflexible mold by applying 100 MPa. Samples were sintered at 1200 °C under 1×10^{-5} Pa. The Ti 3D porosity is assured by controlling the particle sizes and shapes as well as the processing parameters.

The morphological characterization of Ti compacts was performed by scanning electron microscopy (SEM) images. Figure 1a depicts the top surface morphology of the sintered Ti compact before the hydrogenation process. Some polygonal plans can be verified in this magnification, which arose during the uniaxial pressing and sintering processes of the titanium substrate productions. These plans contributed to the emergence of a step-like structure characteristic of the Ti compacts produced by the P/M technique. This step-like structure is probably originated from the volume shrinkage during the compacting and sintering processes [65].

In order to have a better visualization of the surface morphology of these Ti compacts, Fig. 1b presents the step-like structure region in a higher magnification. It is possible to observe that this structure is formed by a micrometric and nanometric sized steps with a smooth surface texture. To compare the Ti surface texture before and after the hydrogenation process, Fig. 1c shows the effect of the hydrogenation process at 600 °C on the Ti matrix top surface morphology. By comparing this image with that presented in Fig. 1b, it is possible to verify that, for the experimental conditions employed, the hydrogenation reactions performed in the HFCVD environment increased the Ti surface roughness. This behavior was observed for all temperatures studied in this study.

Considering the HFCVD conditions, we believe that, as the atomic hydrogen reaches the atoms in the Ti surface, a rapid diffusion process occurs and the reaction among the radical species gives rise to the precipitation of titanium hydrides (TiH_x) compounds. The central part of Fig. 1c shows a region of the hydrogenated Ti compact where these tiny needles become discernible. The needles are well visible in Fig. 1d with higher magnification.

The results presented above are in agreement with that presented by Chen et al. [66]. They showed that, in alpha matrix, the presence of the hydrogen promotes the production of titanium hydrides species with an increase in the size and volume of the precipitated hydride. Therefore, the precipitation of the more voluminous TiH_x compounds on the Ti matrix in HFCVD conditions as well as a misfit between them generated a significant change on the Ti surface, increasing its roughness. Taking into account that

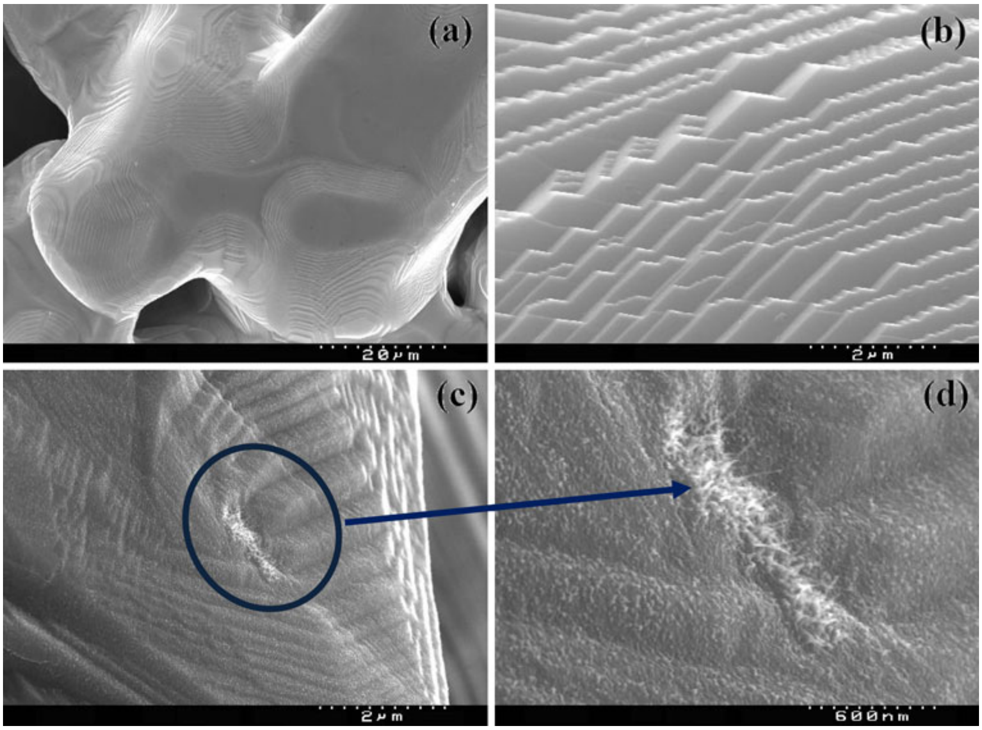

Fig. 1 SEM Images of the Ti compact with 3D porosity: **a** general view of the non-hydrogenated Ti compact surface; **b** surface texture of the non-hydrogenated Ti compact in higher magnification showing the step-like structure formed; **c** general view of the Ti compact surface hydrogenated at 600 °C, and **d** surface texture of the Ti compact hydrogenated at 600 °C in higher magnification evidencing the needles of the TiH_x compounds

the diamond growth environment is formed by high concentration of hydrogen species [36, 67], these results indicate a link between the morphology of the diamond film and the increase of the roughness in the titanium surface during the CVD-diamond growth.

Grazing incident X-ray diffraction (GIXRD) spectra of the samples were collected in the incident angles of 1°, 3°, and 15° recorded in the coupled θ–2θ peak integration mode throughout the range from 30 to 100°. Figure 2 shows the spectra for the hydrogenated samples at temperatures of 500 (Fig. 2a), 600 (Fig. 2b), 700 (Fig. 2c), and 800 °C (Fig. 2d), at 3° incident angle. These spectra show the main peaks related to the reflections of the TiH_x phases in the whole range of temperature studied.

A careful analysis of the spectra presented in Fig. 2 easily identified the dominant diffraction peaks corresponding to the TiH stoichiometries. This makes it possible to identify this phase as the predominant one in the one-hour hydrogenation time. It is important to point out that, in all diffraction angles studied, the amount of hydrogen that reacts with the Ti matrix to form TiH phase increases with the temperature. As a consequence, the TiH_x concentration increased as the Ti surface roughness also increased. Thus, it is possible to control the CVD-diamond grain size controlling the hydrogenation degree of the Ti sample before or during the CVD-diamond growth process.

The influence of experimental parameters on CVD-diamond growth into 3D titanium matrix

In order to growth diamond films on/into 3D porous Ti metallic matrices by the HFCVD technique the control of experimental parameters is very important. They are responsible for the quality, the morphology, composition, and the physical–chemical properties of the films. The following sub-sections will describe the influence of the experimental parameters to obtain such films.

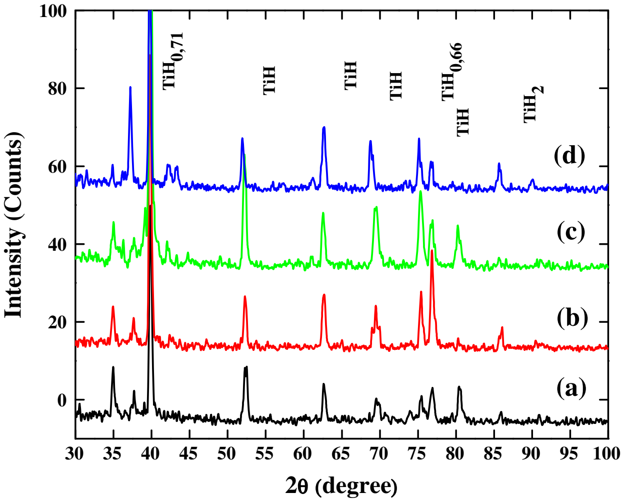

Fig. 2 XRD obtained at 3° incident angle as a function of the hydrogenation temperature: *a* 500 °C; *b* 600 °C; *c* 700 °C; *d* 800 °C

Diamond films on 3D porous Ti as a function of pressure variation

During the growth process, the pressure inside the reactor may influence the film morphology, the quality and the nucleation rate [68, 69]. Figure 3 shows the surface SEM images for diamond/porous titanium surfaces deposited at 2.67 kPa (Fig. 3a), at 4.67 kPa (Fig. 3b), and at 6.67 kPa (Fig. 3c). The 4-h-growth time, the substrate temperature at 600 °C and the CH_4 concentration of 1.0 vol% were kept constant. The images show that for lower pressures at 2.67 and at 4.67 kPa the diamond morphology is formed by well-faceted crystals with (111) and with (100) orientations. For high pressure value at 6.67 kPa, the film morphology changed to a “cauliflower like” formation with smaller grains, mainly attributed to a secondary nucleation process, caused by the high nucleation rate in the first stage of the film growth. The pressure effect, particularly for the film deposition on tridimensional substrates, is associated with the free path way of radicals present in the gas phase that increases as a function of pressure decrease. This behavior contributes to the increase of the etching rate. Consequently, the increase in the active sites on the substrate surface permit’s the production of a large number of such radicals present in the inner titanium surfaces and holes that are far from the filaments.

In this way, the pressure effect becomes very important to grow diamond films on porous Ti. Figure 3d–f represents the deeper surfaces of this substrate that are also coated (as expected) by diamond film, corresponding to the three pressures studied at 2.67, at 4.67, and at 6.67 kPa, respectively. The best diamond formation is clearly identified for the film obtained at the lowest pressure, where even the internal surfaces, the edges, the bottom holes, the good quality as well as the continuous diamond coating was observed (Fig. 3d). This film performance is associated to the highest amount of active sites available for the diamond nucleation when the lowest pressure is kept inside the reactor.

The sp^2/sp^3 ratio was measured as the “purity index” (PI) from Raman spectra by the following equation [70]:

$$\mathrm{PI} = \frac{I_D}{I_D + \frac{I_c}{50}},$$

where I_D and I_C correspond to the integrated Raman peak intensity of diamonds at around 1332 cm^{-1} and to the non-diamond carbon phases at 1350 and at 1550 cm^{-1}, respectively.

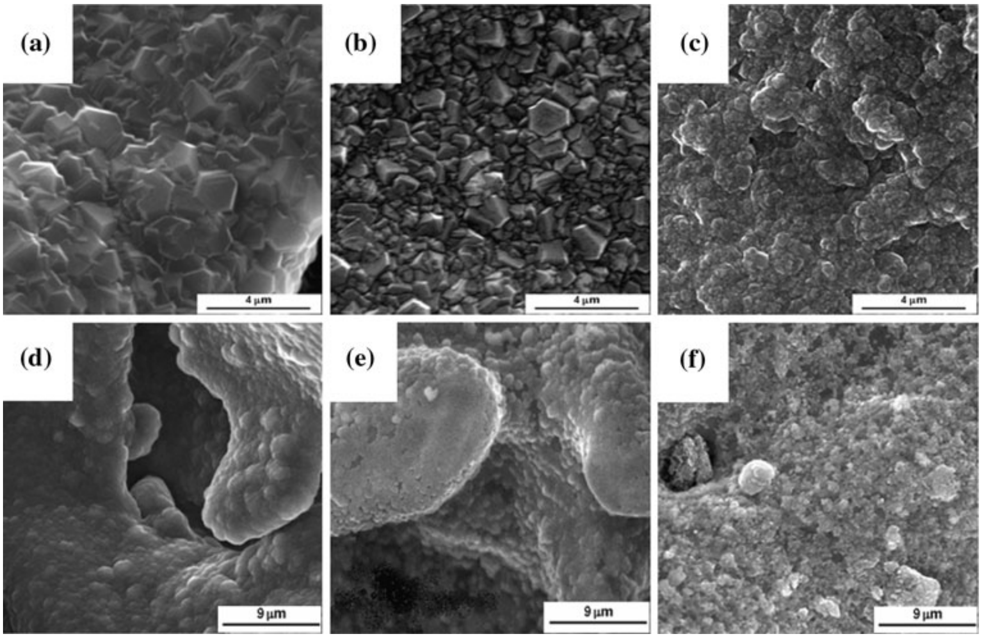

Fig. 3 SEM images of the CVD-diamond films grown on pure porous Ti substrates. The growth time of 4 h, substrate temperature at 600 °C and CH_4 concentration of 1.0 vol% were kept constant: **a**, **d** 2.67 kPa; **b**, **e** 4.67 kPa; and **c**, **f** 6.67 kPa. (**a–c** are respective to top surface images; **d–f** are related with more internal planes)

Likewise, the film crystallinity and its phase compositions were estimated by X-ray diffraction (XRD). The free carbon radicals produced during the gas-phase reactions that reaches the substrate surface involve either the formation of TiC through bulk diffusion into the titanium phase, or take part in the diamond film formation by surface diffusion. Some of these radicals are also used to form non-diamond carbon phases, but they are not detected by XRD measurements. The amount of carbons in the TiC phase and in the diamond phase was evaluated by the "growth tendency index" GTI,

$$\mathrm{GTI} = \frac{A_{\mathrm{D}}}{A_{\mathrm{TiC}}},$$

where A_{D} and A_{TiC} are, respectively, the sum of the intensity integrated area of the diamond peak (111) and the TiC peaks (111) and (200) in the range from 34 to 45°. The GTI can give information on the competition of available carbon atoms between surface diffusion and bulk diffusion.

Figure 4 shows that the PI maximum is obtained at 2.67 kPa. This PI indicator confirms that the highest pressure value induces the lowest film quality. The decrease in the film quality may be explained by the high nucleation rate necessary to form the "cauliflower like" morphology, which introduces a negative effect on the diamond growth with a large number of defects and non-diamond phase in the diamond film [71].

For the deposition to take place, a competition process using these carbon species occurs between the surface diffusion to form diamond and the diffusion into Ti matrix to form TiC. According to the XRD analyses, the present phases associated to their relative intensities were evaluated as a GTI indicator, considering the surface as well as the interface contributions. Figure 4 shows an inversion in the GTI values when compared with the PI. By increasing the pressure, the tendency of the diamond growth is higher than that to form the TiC. When the diamond film starts to grow the carbon diffusion in the titanium matrix becomes more difficult and the TiC formation decreases. In this stage, the diamond formation is dominant and explains how the GTI increase as a function

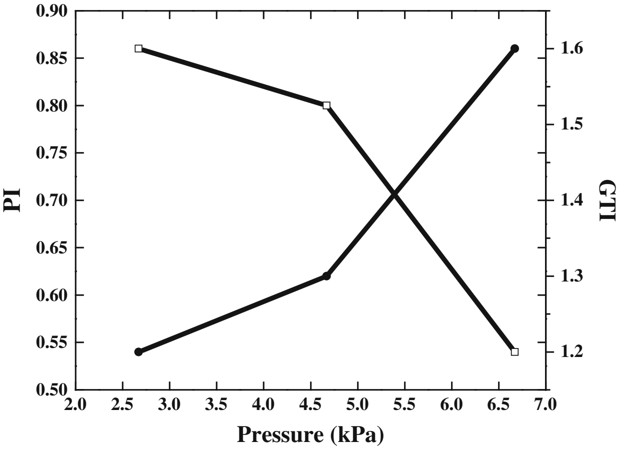

Fig. 4 Dependency of the "purity index" (PI) and "growth tendency index" (GTI) with the total gaseous pressure

of the pressure. To sum up, the pressure at 2.67 kPa was the best value to grow diamond on porous Ti substrate.

Diamond films on 3D porous Ti as a function of the methane concentration

The methane concentration also presented a significant contribution to the morphology and the quality of the film. Figure 5a–e shows the morphology evolution on the surface external for the films grown at different methane concentrations at 1.0, 1.5, 2.0, 2.5, and at 3.0 vol% CH_4, respectively, whereas the images (f–j) represent the morphologies of their inner surfaces and holes. The dominant feature seen in Fig. 5 is the drastic grain size reduction (for a same methane concentration) starting from the external surfaces to the internal surfaces. Another important feature is the grain size reduction in the external and the internal surfaces as the methane concentration was increased. Such effect were more pronounced when the methane concentration were changed from 1.0 to 1.5% CH_4. Moreover, the (100) orientation became more evident for film with 3.0 vol% CH_4. It is known that in HFCVD reactors the diamond nucleation density on silicon substrate increases with the methane concentration increase [72, 73]. The secondary nucleation increase is also observed in the inner surfaces, mainly for films grown with 1.5 vol% CH_4 (Fig. 5g) where the nanocrystalline morphology became dominant in the inner substrate regions.

A more detailed investigation showed that, for the inner surfaces, where the gaseous composition is rarefied, the "cauliflower like" morphology was dominant. This behavior was associated with the nucleation rate influenced by the gas phase. Haubner and Lux [74] have argued that, at temperature depositions lower than 800 °C, the microstructure formed by faceted diamond is dominant for methane concentrations lower than 8 vol%. These results are in good agreement with our results for the external surfaces of the films. Otherwise, for the substrate inner regions (images f–j) a governing factor to form the "cauliflower like" morphology is the low concentration of atomic hydrogen and carbon radicals, which directly influenced the sp^2 carbon etching and the TiC formation, respectively.

Figure 6 shows a crescent increase in the "purity index" (PI) for films grown up to 2.0 vol% CH_4. The PI indicator decreases in the upper and lower ranges of methane concentration. The methane concentration is related to the C and the H concentration ratios on the substrate surface [75]. For methane concentrations lower than 1.0 vol%, an insufficient carbon radical numbers were produced during the reaction in the gas phase. Consequently, in some regions of the growth surface the C/H ratio was low and the diamond did not form as a continuous coating. This behavior was observed for film grown at 0.5 vol% of CH_4 (image not shown). For methane concentrations higher than 1.0 vol% of CH_4 a large number of carbon radicals were produced and reached in the growth surface leading to a high C/H concentration ratio. Owing to the high affinity between carbon and titanium, the high carbon concentration makes easier the TiC formation. The high amount of non-diamond carbon increased because the atomic hydrogen etching was not effective for sample grown at 2.5 vol% of CH_4. Furthermore, the GTI decrease showed that the carbon diffusion to form TiC predominated over the diamond formation for this methane concentration. This result permits to associate the secondary nucleation process with the dominance in the TiC formation. In addition, for film grown with 3.0 vol% of CH_4, the huge amount of carbon on the gas-phase commanded the non-diamond phase formation which was directly observed in the PI decrease.

It is well-established in the CVD-diamond growth that, by increasing the methane concentrations the nucleation density, as well as the film thickness also increase. Therefore, for methane concentrations higher than 2.0 vol% of CH_4 it was expected a not easy hydrogen diffusion throughout the Ti substrate. As showed in Sect. 1, the Ti hydrogenation process contributes to increase the cracks formation throughout the entire Ti bulk. The presence of cracks in the diamond films observed in Fig. 5i, j images indicates that the higher methane concentrations were insufficient to avoid the substrate hydrogenation process. At this point it is assumed that the cracks formation in the diamond film is related with the cracks formation in the Ti substrate bulk due to the hydrogenation process. This is not completely understood yet. In this sense, the cracks were more evident to internal surfaces than those for external surface and there is not a complete explanation for this behavior. From our results, the methane concentrations between 1.0 and 2.0 vol% of CH_4 were chosen as more suitable. In summary, the diamond growth on porous Ti substrate is a complex process, and further investigations must be done.

Diamond films on 3D porous Ti as a function of the temperature

Some studies published in the literature dealing with the diamond deposition on titanium substrates have linked the cauliflower-like microstructures to the increase in the TiC formation at high temperatures [43, 76]. These studies pointed out that the temperature exerts a strong influence on the composition of the diamond/Ti interface and, consequently, on the film morphology. Therefore, in this subtopic, the growth of diamond films as a function of the substrate surface temperature is treated in detail. The

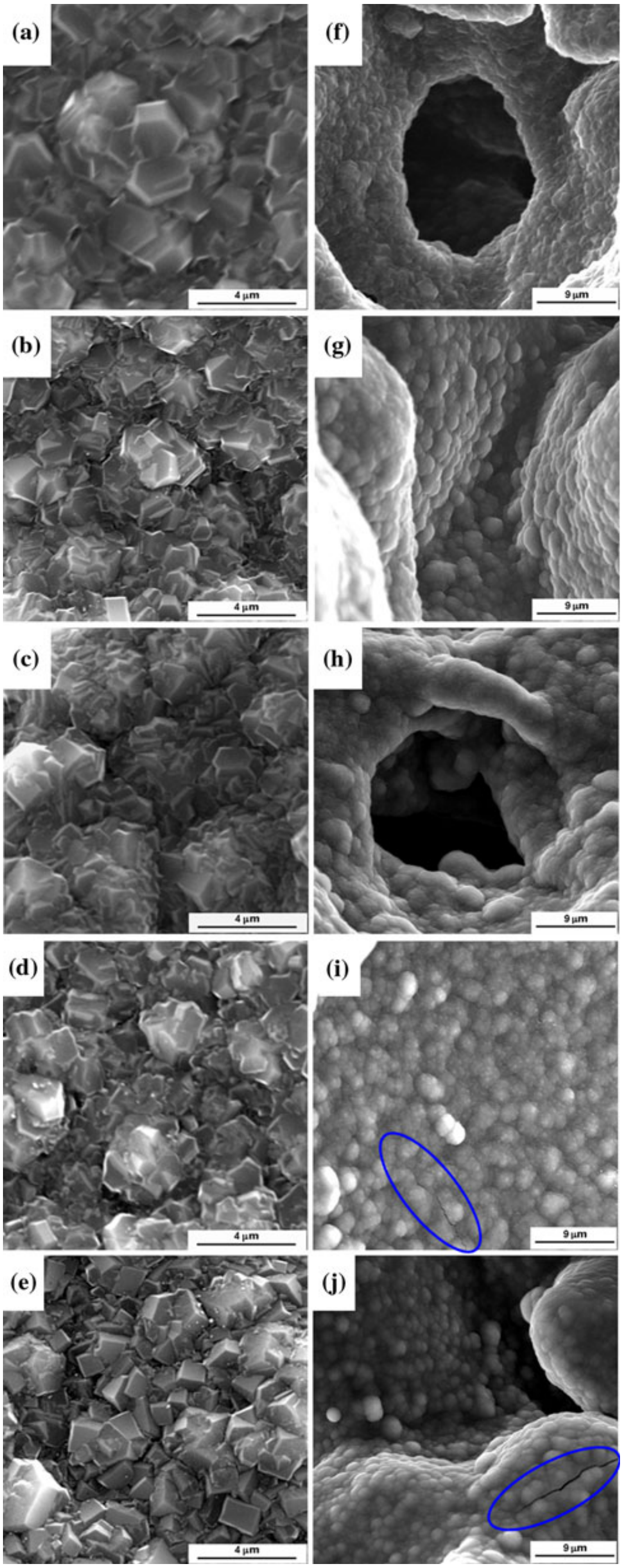

◀ **Fig. 5** SEM images of the CVD-diamond films obtained at different methane concentrations. The pressure of 2.67 kPa, substrate temperature at 600 °C and CH_4 concentration of 1.0 vol% were kept constant. Top surface images: **a** 1.0%; **b** 1.5%; **c** 2.0%; **d** 2.5%, and **e** 3.0%. More internal plane surfaces: **f** 1.0%; **g** 1.5%; **h** 2.0%; **i** 2.5%, and **j** 3.0%. The *circled* areas in images in (**i**) and (**j**) evidence the fissures in the respective films

composition of the phases formed between the diamond film and the substrate surface is pointing out, particularly, the TiC and TiH_2 formations.

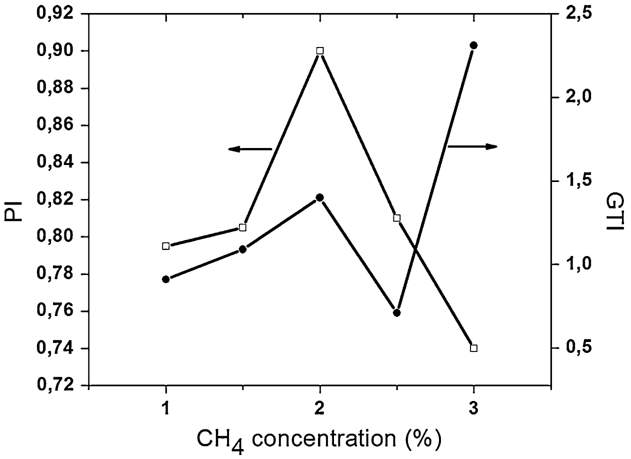

Fig. 6 Dependency of the "purity index" (PI) and "growth tendency index" (GTI) with the methane concentration

The top view SEM images of the diamond films deposited on 3D Ti substrates at 500, 600, 700, and 800 °C are depicted in Fig. 7a–d. By Changing the substrate surface temperature, different textures of the diamond film are also possible [71, 74, 77, 78], which is mainly related to the nucleation and the growth rate variation, which strongly affect the grain size and the film agglomerate formation. A change from the microcrystalline diamond grains with a random crystallographic orientation (at 500 and at 600 °C) to nanocrystalline diamond grains (at 700 and at 800 °C) is observed. The temperature range between 600 and 700 °C seems to be a transition region where these morphological changes take place. This behavior is depicted with more details in Fig. 7b, c insets as well as their considerable grain size reduction.

The morphological changes observed by SEM analyses are also reflected on the Raman's features. These spectra were useful in following the transition from the MCD to the NCD. The CVD diamond often contains appreciable amounts of non-diamond carbon that exhibits characteristic The Raman bands of graphite or of highly disordered sp^2 and sp^3 carbons. The Raman spectra taken from different surface temperatures are reported in Fig. 8a 500 °C, b 600 °C, c 700 °C, and d 800 °C. The Raman spectra, in general, show an sp^2-related contribution for the G and the D bands at 1580 and at 1350 cm^{-1}, respectively. The G peak is related to the E_{2g} graphite mode, whereas the D mode is related to a zone-edge A_{1g} mode of disordered

Fig. 7 Top view SEM images of diamond/Ti composites obtained at different temperatures: **a** 500 °C; **b** 600 °C; **c** 700 °C; **d** 800 °C

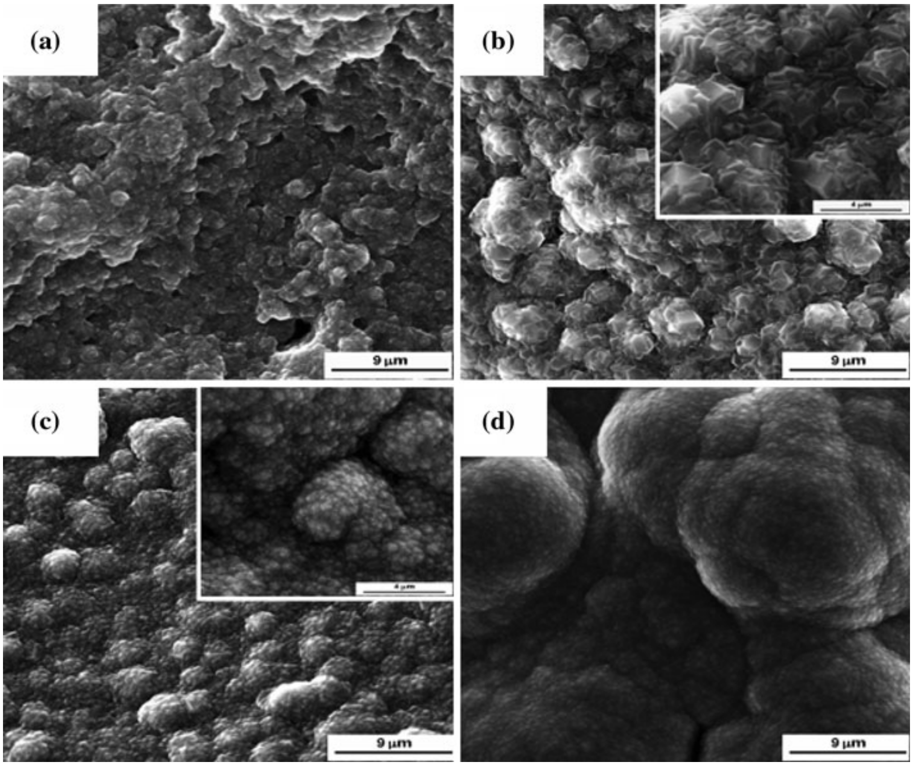

graphitic-like sp^2-bonded carbon [79]. In order to distinguish the different peak contributions we now comment on some general features observed in the experimental data.

Figure 8a shows a narrow band at 1332 cm^{-1}, which corresponds to the diamond (sp^3-bonded carbon) peak. Besides, the presence of the G band is also clear. Figure 8b shows a well-defined peak at 1332 cm^{-1} which corresponds to the best diamond film of this sample set. Figure 8c, d shows a similar behavior. The only slight difference is related to the presence of the diamond peak. Figure 8d has no apparent diamond peak and consists of broadening D and G peaks at around 1350 cm^{-1} and at 1580 cm^{-1} confirming that the non-diamond phase is indeed amorphous. A shoulder or a peak is observed at around 1150 cm^{-1}. The evidence for the NCD has been associated with this shoulder Raman line and an additional mode at approximately 1470 cm^{-1} where both are thought to be originated from the sp^2 carbon. The fact that the 1150 and the 1470 cm^{-1} modes appear and shift together suggests that they have the same origin and are associated to the *trans*-polyacetylene (TPA) molecules trapped at the nanograin boundaries [80, 81]. Based on these spectra, the resonant enhancement of the sp^2 portions ($\sim$1580 cm^{-1}) of the film are strongly dependent on the deposition temperature. However, it is impossible to determine if the observed results were only due to the resonant part of sp^2, or in fact, there are some other mechanisms that move down the G peak in energy and skew it. These mechanisms may be associated to the intermediate phases and/or to the defects that affect the diamond film formation. Most of the results presented here have the important implications for the CVD-diamond film morphology. By increasing the surface temperature the Raman active bands in nanocrystalline systems reflect contributions to the entire Brillouim zone leading to the broadening of the diamond band as the nanocrystallite size decreases.

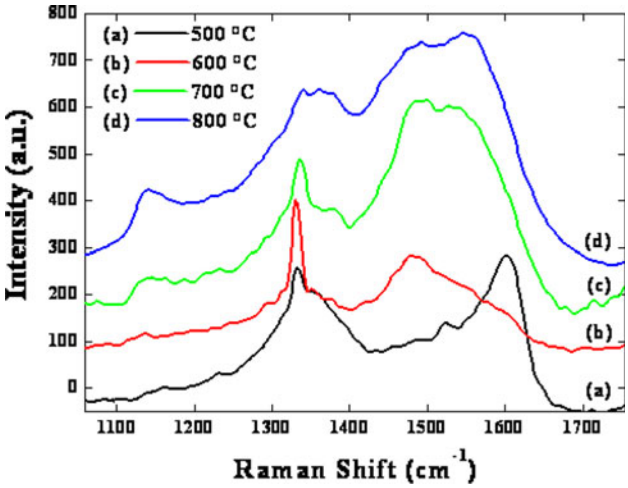

Fig. 8 Raman spectra of diamond/Ti composites obtained at different temperatures: *a* 500 °C; *b* 600 °C; *c* 700 °C; *d* 800 °C

The characterization of the coating crystalline structure was obtained by GIXD. To investigate the complex structure of the diamond/Ti samples, full diffraction patterns were collected. The XRD spectra obtained in the range from 30° up to 80°, allowed us to evaluate the TiH_2 (110), the TiC (111), and the TiC (200) phases (Fig. 9). The GIXD spectra obtained at different temperatures confirm the occurrence of diamond structures at 44° and at 75° corresponding to the C (111) and the C (220) diamond diffractions, respectively. The complete deposition sequence takes about 6 h, and the diamond crystallites form a continuous coating which develops both in thickness and in orientation. As far as characteristic features of diamond phases seen in the XRD spectra are concerned, the diamond coating are different and show a strong dependence on the temperature.

The experimental findings indicate that the substrate temperature generated several intermediate phases that contribute to the diamond morphology. The combined use of the GIXD, of the Raman spectra and of the SEM techniques allowed us to understand the structure of the intermediate phases and its contribution to the diamond morphology. As far as the relative structure of the intermixed phase is concerned, the GIXD patterns show that there is a progressive inversion in the intensities of the TiH_2 (111) and the TiC (200) phases with the substrate temperature. The GIXD patterns obtained at an increasing incident angle from 1° to 15° confirmed the formation of titanium hydrides beneath the diamond coating and the titanium carbide layer.

Figure 9 shows the XRD spectra obtained at different temperatures at the incident angle of 15°. The formation of the TiC phase was detectable for all temperatures studied, and it was observed that the TiC peak became stronger with the increase in the temperature surface. During the CVD process, carbons will react with the surface Ti atoms to form carbide grains. However, as the titanium carbide layer reaches a critical thickness, a further growth of the carbide phase is limited by the titanium capability to be out-diffused from the substrate through the layer itself. According to the model proposed by Terranova et al. [82], the mixed Ti carbide/hydride phase is deposited into the hollows, and graphite is formed on the surface protrusions, in the early stages as clusters, and then, it is covered with the carbide. In the present experimental conditions, no graphite peak is discernible in the XRD spectra, indicating the nonexistence of any substantial amount of crystalline graphite at the beginning of the diamond film deposition.

The diamond film formed at 500 °C on a mixed TiC/TiH_2 layer is characterized by the presence of hydride grains oriented prevalently along the $\langle 111 \rangle$ direction. A further increase in the substrate temperate at 600 °C the TiC phase is enhanced, and the TiH_2 (111) phase is almost halved (Fig. 9). The diamond film at this temperature also shows an increase in the nucleation density. The reason probably lies in the fact that the diamond phase nucleation is a process competing with the carbide formation. At this temperature, the TiC layer did not reach a critical thickness, as can be seen in Fig. 10. As a consequence, the carbon from the gas phase may either accumulate on the substrate surface to nucleate sites to be a precursor to diamond formation or diffuse to into the Ti matrix. The hydrogen diffusion into the substrate and the growth of hydride phase are found to compete with the titanium carbide formation, mainly in the hollows of the substrate, where the reduced concentration of carbon species avoids the formation of thick carbon clusters.

By increasing the substrate temperature, a secondary nucleation rate led to a development of the predominant cauliflower structures. The growth mechanism changes from MCD to NCD. The critical zone is the temperature range from 600 to 700 °C because the hydrides tend to decrease and carbides to increase. This temperature range

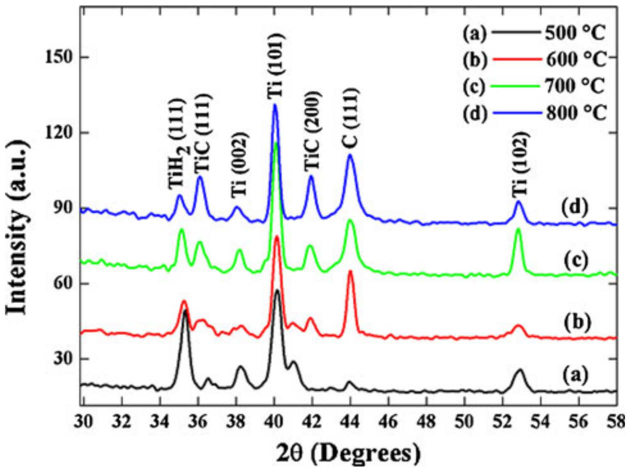

Fig. 9 XRD patterns, collected in the 15° incident angle, at different substrates temperatures: *a* 500 °C; *b* 600 °C; *c* 700 °C; *d* 800 °C

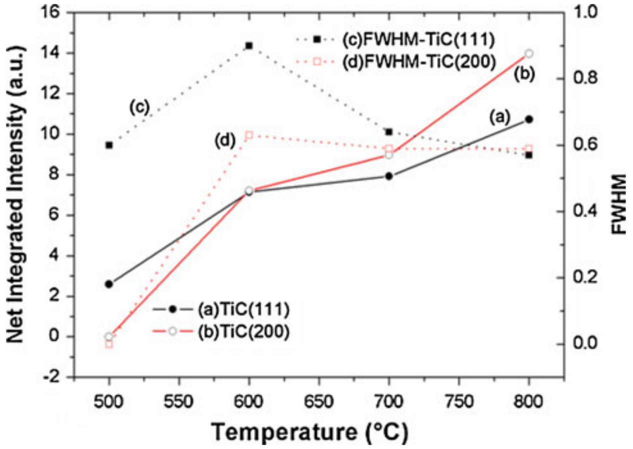

Fig. 10 Net integrated intensity and FWHM as a function of the substrate temperature on *a* TiC (111), *b* TiC (200), *c* FWHM-TiC (111), and *d* FWHM-TiC (200)

seems to be a transition region where these morphological changes take place. This behavior is depicted in Fig. 7c, d. At this stage, it has been confirmed that the temperature influences the interface composition. The interfacial layer evolves through a gradual transition from a mixed phase titanium-hydride/-carbide in the temperature range from 500 to 600 °C to titanium-carbide, and to TiC (111) and TiC (200) in the temperature range 700–800 °C.

Concerning the structure of the interfacial layers, the investigations of full width at half-maximum (FWHM) values obtained for the TiC (111) and the TiC (200) indicate a decrease in the TiC crystallinity from 500 to 600 °C. Otherwise, its increase was observed from 600 to 700 °C (Fig. 10). It is noteworthy that FWHM values showed a trend variation in the crystallinity from 700 to 800 °C. The net integrated intensity presents a continuous formation of the TiC phase as a function of the temperature. The increase in the intensity values for both (111) and (200) TiC phases characterizes a competitive process. So, the diamond phase nucleation became competitive due to the temperature increase which is associated to the carbide formation. The TiC phases under the effect of atomic hydrogen provide the broadening of the Raman peak that is evidenced in the range from 700 to 800 °C and also create highly reactive surface. The role of the hydrogen atoms is crucial in the deposition process, since the H can etch the surface of the graphitic carbon and help to terminate the dangling bonds. Besides, the H radicals split the hydrocarbon in a gas phase. The H radical concentration at the growth surface is very important to efficiently perform all the reactions necessary for the diamond growth. By increasing the substrate temperature, the thermal energy of the free carbon radicals on the surface also increases enhancing the carbon diffusion rate. This process results in the increase in the carbon concentrations and leads to a high reactive surface. It is important to remember that the abundance of carbon species explains the tendency to form nanodiamond or graphite. Besides, the diffusion could also be enhanced by the formation of defects and dislocations. These defects can be associated with abundant graphitic carbon formation and other phases as indicated by the broadening of the Raman peak.

Diamond films on 3D porous ti as a function of the Argon concentration

The MCD and NCD diamond films were grown on 3D porous Ti substrates at 600 °C varying the argon concentration from 0 to 90 vol% for a fixed methane concentration of 1.5 vol% in a balanced Ar/H_2 flux of 100 sccm. The comparative SEM micrographs showed that there were significant changes in the diamond grain sizes and the film surface morphologies due to the continuous argon addition to the gas mixture. The images show that, as the Ar concentration increases, the microstructure continuously changes from well-shaped grains with sharp facets (Fig. 11a) to a smooth cauliflower-like structure (Fig. 11b–d) also typical for NCD films. For Fig. 11a, the dominant structure is the typical microcrystalline diamond on the Ti substrate, with average grain sizes lower than 1 μm, characteristic of films with high nucleation rate.

The films grown with 40 vol% Ar (Fig. 11b) presented smaller grains, already presenting a cauliflower-like structure, formed from large agglomerates, which defined submicrometer crystallites with a fine texture. This behavior suggests a secondary nucleation or renucleation process. Small grain densities increase significantly at the level of 70–90 vol% Ar (Fig. 11c, d). For the films grown with 70 vol% Ar, the grains tend to form agglomerates that become more pronounced than those formed with 90 vol% Ar. The NCD films with agglomerates grown on the silicon substrate were also obtained by Yang et al. [83]. They observed the cauliflower-like diamond formation, for the Ar concentrations above 30 vol%. They stated that the cauliflower diamond is nearly a pure diamond with strongly twinned microstructure that grows at the transition from faceted diamond to graphite depositions. This morphology is clearly observed in the images of Fig. 11b–d.

The morphological changes observed by the SEM analysis are also reflected on the Raman spectra features (Fig. 12). The components of the characteristic diamond Raman's peak at 1332 cm^{-1}, a peak at 1350 cm^{-1} (D peak), and a G peak centered at 1580 cm^{-1} can be observed [79]. The TPA peaks at 1150 and 1470 cm^{-1} are also presented. The spectrum (a) in Fig. 12 is particularly related to the diamond film obtained without argon addition to the gas mixture, i.e., using the standard composition for the MCD deposition. Despite the standard MCD conditions, the *t*-polyacethylene peaks associated to the NCD coatings are observed. This NCD formation may be attributed to the poor concentration of atomic hydrogen in the substrate holes, which represents deeper planes in relation to the filament distance, leading to a lower diamond growth rate. Thus, the contribution to the diamond layers formed in the Ti holes becomes representative on spectrum 12a generating the observed NCD feature. They presented smaller grain size than those on top of the Ti surface. Furthermore, the spectra of Fig. 12b–d are related to the diamond films grown with the Ar concentrations of 40, 70, and 90 vol%, respectively. These spectra are consistent with those expected for the NCD films [84]. As the diamond thin films undergo a transition from the MCD to the NCD morphology, the Raman spectra became dominated by the scattering of the sp^2-bonded at the diamond grain boundaries [85]. The Ar increase affected the shape

Fig. 11 Top view SEM images of the diamond/Ti composite obtained with **a** 0 vol%, **b** 40 vol%, **c** 70 vol%, and **d** 90 vol% of Ar concentration in the precursor mixture, respectively

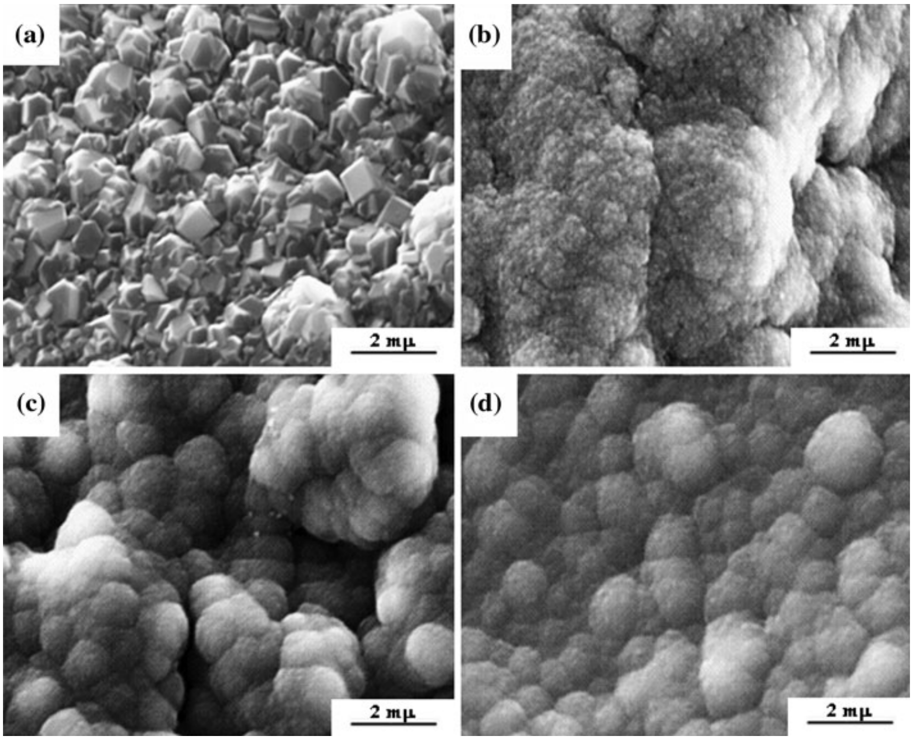

of the narrow diamond peak, which is generally, obscured by the D band overlapping and it is also more sensitive than the diamond phase for the NCD films when the visible Raman spectra are used.

The XRD patterns of the diamond surfaces are shown in Fig. 13 for the films grown without Ar and with 90 vol% Ar, respectively. The XRD spectra of the MCD/NCD films clearly present the peaks at 44° and 75.5° corresponding to the (111) and (220) diamond diffractions confirming the diamond crystallinity presence [76, 86]. The diffraction pattern (a), related to the MCD film, presented a small shoulder close to the Ti (101) peak, which may be attributed to small amounts of titanium-hydride formation. This presence was not detectable for the films grown with Ar addition, probably associated to the reduction of hydrogen content in the gas mixture. In addition, apart from the

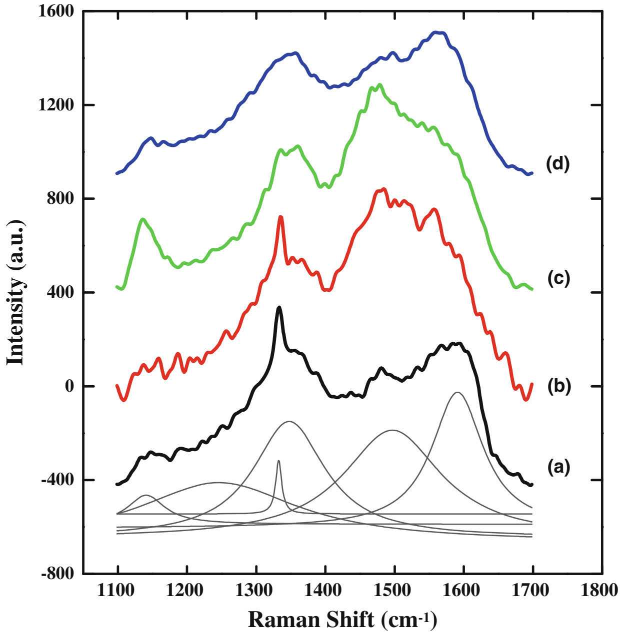

Fig. 12 Raman spectra of MCD and NCD films grown with *a* 0 vol%, *b* 40 vol%, *c* 70 vol%, and **d** 90 vol% of Ar concentration in the precursor mixture, respectively

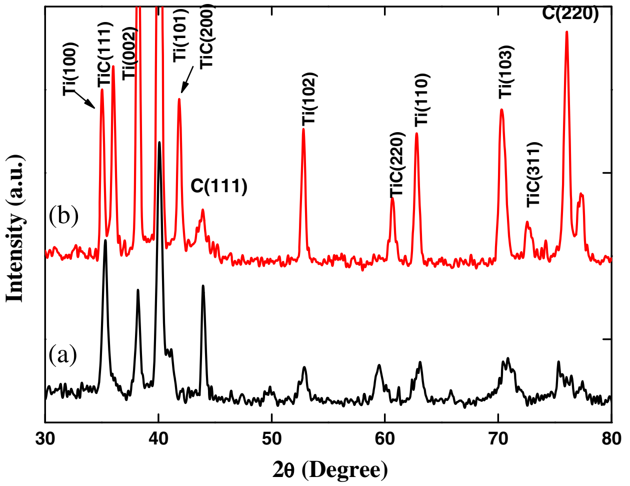

Fig. 13 XRD patterns of MCD and NCD films grown at two different Ar concentration *a* 0 vol%; *b* 90 vol%, respectively

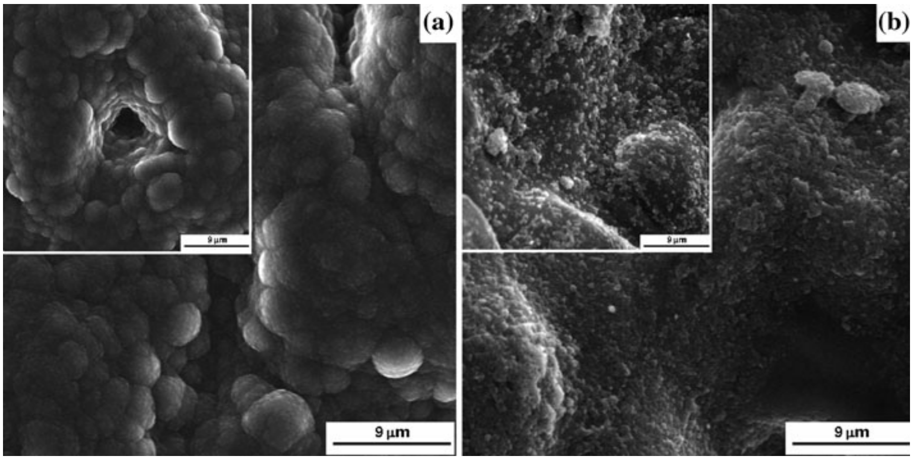

Fig. 14 SEM images of the diamond film grown with RVC 2000 °C heat-treated as the only carbon source: **a** Top surface morphology; (**a**, *inset*) morphology of the hole located at the top surface; **b** Bottom surface morphology; (**b**, *inset*) morphology of the hole located at the bottom (opposite side of the sample)

recognized Ti peaks, the most usual TiC formation is clear, related to the (111), (200), (220), and (311) peaks.

As the Ar gas was added to the reactant atmosphere, the microstructure of the films exhibited a drastic change. The high secondary nucleation rate led to a development of the predominant cauliflower-like structures. Concerning the (111) and (220) reflections, it is worth noting that there is an inversion in the intensities of these diffraction peaks (Fig. 13a, b) caused by the growth mechanism change from the MCD to the NCD. Silva et al. [86] have rationalized the preferential ⟨110⟩ orientation in the NCD film formations in terms of the fastest growth direction of the single crystal and the formation of micro-twinning on the (111) planes. According to them, the growth rate of the planes (111) is enhanced by the formation of micro-twinning on them providing the nucleation sites at the re-entrant corners. As a consequence, a competition between the growth of the (111) and the (110) planes might occur. They have shown that this competition is more favorable to the emergence of a ⟨110⟩ texture and provides a growth model whose main concept is the development of the cauliflower-like particles formed by the nanometric growing sectors elongated along the ⟨110⟩ axis.

One-step HFCVD-diamond coating process using a solid carbon source

There are some works in the current literature that have discussed the diamond deposition with high growth rate [87] and good quality using a solid additional carbon source just below the substrate, [88, 89]. In these works, the additional carbon source was enough to supply the necessary hydrocarbon for the efficient nucleation rate required for the diamond growth infiltration without the bottle neck effect with a reduced diamond growth time [90, 91]. This bottle neck effect results from the decrease in concentration of atomic hydrogen and pertinent growth species in the pore. The pore mouth gets closed at first by the overgrowing diamond coating at the surface. This makes a complete infiltration difficult. As a consequence, the pore mouth is closed before the pore is completely infiltrated.

Nevertheless, there are no reports exploring the growth of the HFCVD films on the Ti substrates by using only a solid carbon source as an infiltration process into deep 3D-Ti substrate. For this purpose, the reticulated vitreous carbon (RVC) samples, obtained at Heat treatment temperature (HTT) at 1300 and 2000 °C were used. The RVC is an open pore honeycomb-like structure which belongs to the turbostratic carbon class, presenting lamellar carbon structure similar to graphite with hybridization sp^2, and making up strips which are randomly organized in space. The different HTT promoted different levels of carbon structural organization on such RVC samples used as a solid carbon source to grow diamond films. The HTT simultaneously influences the structural organization as well as the chemical surface of the RVC. Previous works have discussed the importance of thermal treatment related to its strong dependence upon the microstructural properties of this material. [92–94].

After the carbonization process, the RVC presents a disorderly porous glassy carbon (GC) structure with some crystallographic order associated with its graphitization index. As far as the RVC1300 is concerned, a major contribution comes from its high oxygen content. The oxygen presence in the gas phase for the diamond growth has already been extensively studied [95] and has shown that the OH formation is more efficient to etch sp^2 and sp^3 bonds than the atomic hydrogen itself. Furthermore, the oxygen presence favors the CO formation from carbon excess provided by the substrate etching. These contributions decreased the film growth rate and favored the highest substrate etching. For the RVC2000 the surface bond does not present an oxygen content, but it presents a structure closer to the graphite arrangement that may facilitate the attack on graphitic structures and are more susceptible to the action of chemical agents as the atomic hydrogen present in the gas phase [96].

The HFCVD-diamond films were grown on porous 3D Ti substrates at 630 °C in argon concentration of 80 vol% in a balanced Ar/H_2 flux of 100 sccm. A piece of RVC (2000 or 1300) was used, just below the Ti substrate, as the only carbon solid source. A distance of 2 mm was kept from the RVC top surface to the Ti bottom surface while the distance from the Ti top surface to the filaments was 6 mm. These experimental conditions insured in a one-step the production and infiltration of pertinent carbon growth species all over the 3D Ti surfaces. It is important to emphasize that, not only the surfaces located on the top (top surfaces) side of the Ti sample, but also that one located on the opposite side (bottom surfaces), were covered by a continuous NCD film. Figure 14a shows the top surface of the SEM image of the diamond film grown with the RVC2000 as the only carbon source.

The dominant morphological aspect presented for this sample is the cauliflower-like structure. This morphology is also present in the film deposited on the pores and cavities of the Ti top surface. Figure 14a shows the film continuity which leads to the formation of a NCD/Ti 3-D material, keeping the original features of the porous Ti compacts with a diamond infiltration in the whole sample. The image also confirms the film continuity even at the strut edges (angular surfaces), where different growth rates are necessary to insure the film adherence. Although the opposite side of the sample presented a less dense agglomerate formation, Fig. 14b shows that this side of the sample is totally covered by a thin NCD film since the Ti hexagonal microstructure is not revealed. This aspect is also present in these sample side cavities (Fig. 14b inset). A comparison between the NCD growth and the two sides of the sample reveals that, for the surface closest to the RVC (bottom surface), the NCD growth rate was lower than that for the top surfaces. This aspect stresses the importance of the atomic hydrogen during the diamond process. Although the top surfaces were more distant from the RVC, they were closest to the filaments where the atomic hydrogen was generated and contributed to the surface etching.

In order to analyze the composition and the quality of the NCD films grown with the RVC as the only carbon source, the Raman spectra were registered. Figure 15a, b presents the Raman spectra of the samples grown with RVC1300, the bottom and the top surface, respectively, and Fig. 15c presents the Raman spectrum of top surface for the sample grown with RVC2000. It may be verified that, for both NCD films, including their bottom sides, the presence of the Raman peak in the 1332 cm^{-1} region corresponding to the diamond phonon vibration, the peak at 1350 cm^{-1} (D peak), and the G peak centered at 1580 cm^{-1} are observed. The TPA peaks at 1140 and 1470 cm^{-1} also appear.

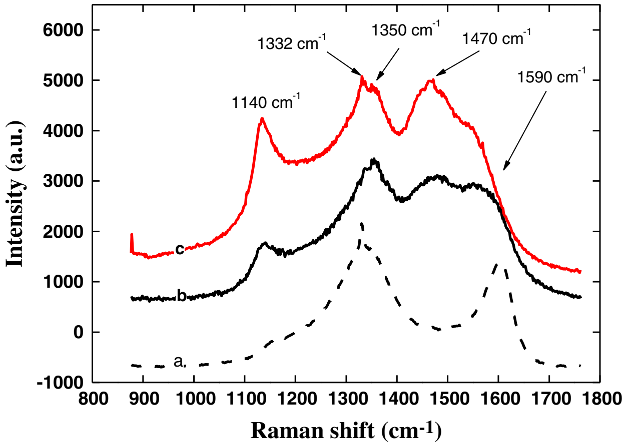

Fig. 15 Raman spectrum of the NCD films grown with: *a*, *b* RVC 1300 °C heat-treated, bottom, and top surface, respectively; *c* RVC 2000 °C heat-treated top surface

By comparing these samples, we can see that there was no significant difference in the growth of the CVD-diamond at the top surface of the samples, since the Raman spectra are similar. However, one major difference is seen when comparing the top and the bottom surfaces of the sample grown with the RVC1300. A large reduction in the intensity of the peaks relating to the presence of TPA is evident. At this point, it is important to remember that the bottom surface of this film was closer to the RVC sample, which presents high oxygen content, while its top surface was located closer to the filaments, where the atomic H was formed. Therefore, this is another evidence that the OH groups were more efficient than the atomic hydrogen in attacking the sp^2 carbon present in the TPA.

Electrochemical characterization of the 3D porous diamond electrodes

In this subsection, the electrochemical characterization of three electrodes obtained by coating of the 3D Ti substrates will be performed. The first electrode nominated 3D/Ti-BDD was obtained by coating the substrate with a boron-doped diamond (BDD) film. This BDD film was obtained from a standard gaseous composition according to subsections Diamond films on 3D porous Ti as a function of pressure variation; Diamond films on 3D porous Ti as a function of the methane concentration, and Diamond films on 3D porous Ti as a function of the temperature. For the second electrode, 3D/Ti-NCD, the diamond film was deposited in the nanoscale as described on the Sect. Diamond films on 3D porous Ti as a function of the Argon concentration, and the third, 3D/Ti-RVC, electrode was obtained by using a solid RVC 2000 °C heat-treated as the only carbon source as described in the Sect. One-step HFCVD-diamond coating process using a solid carbon source.

The electrochemical measurements were carried out using a three-electrode cell. The 3D/Ti porous diamond electrodes were used as working electrodes. Platinum was used as the counter electrode and a commercial Ag/AgCl electrode (3.0 mol L^{-1} KCl solutions) served as the reference. The working electrodes were not submitted to surface pretreatment before the measurements. Cyclic voltammetry used for the electrochemical characterization with the KCl solution (working potential window) and $Fe(CN)_6^{4-/3-}$ redox system for the electron transfer kinetic study of 3D/Ti porous diamond electrodes.

Figure 16 presents the cyclic voltammetric curves for 3D/Ti-BDD, 3D/Ti-NCD, 3D/Ti-RVC, and Pt electrodes in 1.0 mol L^{-1} KCl solution. The voltammetric behavior indicated that the 3D/Ti-BDD, the 3D/Ti-NCD, and the 3D/Ti-RVC electrodes present a working potential window of approximately 3.3 V versus Ag/AgCl. This value is similar to that already described in the literature for BDD and NCD films deposited on silicon [81, 97], but much broader when compared with others commonly used as electrode materials, such as, platinum (~2.0 V, see Fig. 16), vitreous carbon (~2.5 V) and graphite (~2.0 V) electrodes [98]. The wide working potential range (up to 3.0 V), presented by these electrodes, defines the higher cathodic and the anodic limits for water decomposition reaction. It represents the main parameters for the detection of many electroactive species in aqueous electrolytes, without the interference of the water reduction and oxidation reactions. For all 3D electrodes, the onset of hydrogen evolution due to water reduction is verified to begin at ~−1.6 V, whereas the onset of oxygen evolution due to the water oxidation begins at 1.7 V. The contribution of the capacitive background current involved in the electric double-layer charging is associated to the surface area exposed to the solution and to the amount of sp^2-bonded carbon impurities exposed at the grain boundaries. According to Show et al. [99] this carbon is a source of π states that contribute to the density of electronic states in the material, increasing the capacitive component of the background current. When compared with platinum electrode (see Fig. 16), all 3D electrodes represent the low capacitive background current, justifying the excellent stability suited for current-based electrochemical measurements. In particular, this characteristic associated with higher anodic limit makes them a superior electrode to be used in electrooxidation of organic species [100]. In this way, these electrodes have been used at wastewater treatments promoting the combustion of organic pollutants with high-current efficiency [101].

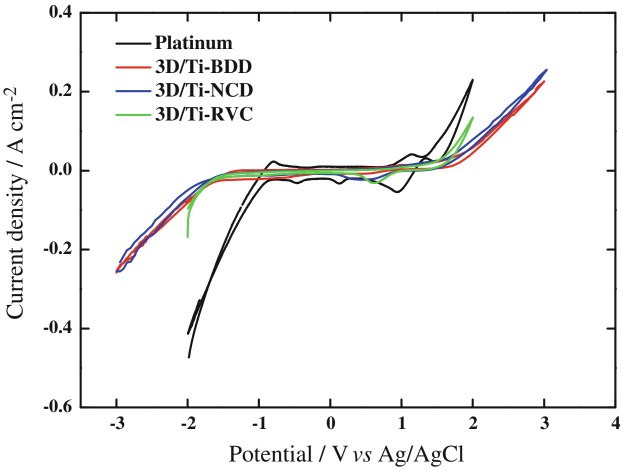

Fig. 16 Cyclic voltammograms for 3D/Ti-BDD, 3D/Ti-NCD, 3D/Ti-RVC, and Pt electrodes in 1.0 mol L^{-1} KCl solution, $v = 50$ mV s^{-1}

The characterization of the working potential window and capacitive currents, from cyclic voltammograms presented in Fig. 16, showed clearly that the properties of diamond films deposited on porous Ti substrate have similar electrochemical properties when compared to the diamond films deposited on silicon substrate. On the other hand, they presented better electrochemical properties than that for the platinum electrode.

Besides the analysis with respect to working potential window and the background currents for electric double-layer charging, it is also common to evaluate the electrode kinetics for occurring of redox reactions through the electrode/electrolyte interface. The $Fe(CN)_6^{4-/3-}$ redox couple is one of the most used for the characterization of diamond electrodes [102], since the electrode reaction kinetics for this redox couple is sensitive to the presence of exposed edge plane on sp^2-bonded carbon in microcrystalline boron-doped diamond and nanocrystalline diamond films. Using this redox couple, kinetic parameters, such as, peak potential separation (ΔE_p), and peak current (I_p) versus square root scan rate ($v^{1/2}$) obtained from cyclic voltammograms can easily be evaluated.

The plots of ΔE_p versus scan rate for the three, 3D/Ti-BDD, 3D/Ti-NCD, and 3D/Ti-RVC, electrodes obtained at 1.0 mmol L^{-1} $Fe(CN)_6^{4-/3-}$ and at 1.0 mol L^{-1} KCl solution are presented in Fig. 17. For all electrodes, ΔE_p increases with the increase of scan rate, but the ΔE_p values obtained for 3D/Ti-RVC electrode were smaller when compared to those for the others electrodes. At low scan rate, the ΔE_p tends to approach of 60 mV for the 3D/Ti-BDD and 3D/Ti-RVC electrodes, whereas for the 3D/Ti-NCD electrode tends to approach of 120 mV. According to the criteria used for testing the electron transfer reaction kinetic [103], the ΔE_p of 59/n mV (where n is the

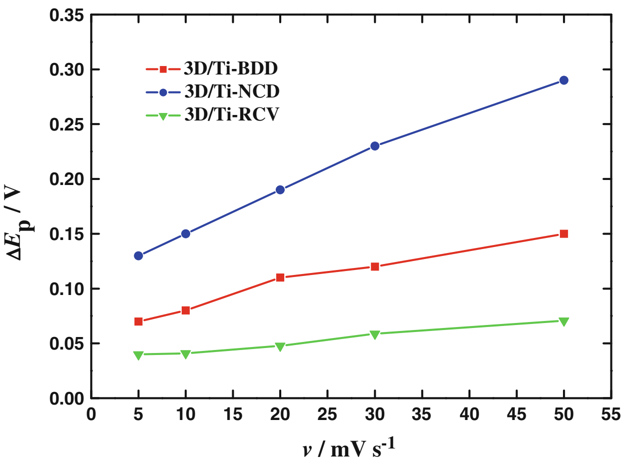

Fig. 17 Plots of ΔE_p versus scan rate for the electrodes 3D/Ti-BDD, 3D/Ti-NCD, and 3D/Ti-RVC obtained in 1.0 mmol L^{-1} $Fe(CN)_6^{4-/3-}$ and 1.0 mol L^{-1} KCl solution

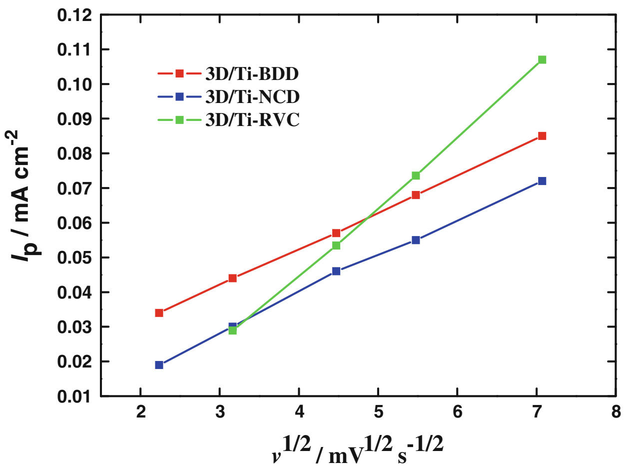

Fig. 18 Plots of I_p versus $v^{1/2}$ for the 3D/Ti-BDD, 3D/Ti-NCD, and 3D/Ti-RVC electrodes obtained in 1.0 mmol L^{-1} $Fe(CN)_6^{4-/3-}$ and 1.0 mol L^{-1} KCl solution

number of electrons involved in the reaction and $n = 1$ for $Fe(CN)_6^{4-/3-}$ redox couple) is one of the indicative of a quasi-reversible system. In this way, the 3D/Ti-BDD and 3D/Ti-RVC electrodes present a quasi-reversible behavior at low scan rates. In general, the ΔE_p difference might be associated to surface microstructure, the presence of surface carbon–oxygen functionalities as well as the surface cleanliness of sp^2-bonded carbon electrodes [104]. In the case of the 3D/Ti-NCD electrode, the ΔE_p increase may be attributed to the presence of a high amount of the sp^2-bonded carbon when compared with the 3D/Ti-BDD and 3D/Ti-RVC electrodes, as observed in the Raman spectra showed in Fig. 12. This high amount of sp^2 site is responsible by the formation of a large content of oxygen terminated on the surface of 3D/Ti-NCD electrode, which has the function of blocking actives sites to occur the redox reactions and, consequently, to promote a decrease of the electron transfer kinetic for this electrode. Granger et al. [102] showed that surface carbon–oxygen functionalities on microcrystalline diamond significantly influence ΔE_p by increasing oxygen content, causing an increase in the peak potential separation. A similar effect was also observed by Fujishima and co-works [105].

Another criterion to evaluate the electrode kinetic is to analyze the behavior of I_p as a function of $v^{1/2}$. The Fig. 18 presents plots of I_p versus $v^{1/2}$ for the 3D/Ti-BDD, the 3D/Ti-NCD, and the 3D/Ti-RVC electrodes obtained at 1.0 mmol L^{-1} $Fe(CN)_6^{4-/3-}$ and at 1.0 mol L^{-1} KCl solution. For all electrodes, it can be seen that I_p varies linearly with $v^{1/2}$ with a near zero y-axis intercept, that is an indicative of reactions limited by semi-infinite linear diffusion of reactants to the electrode surface. Despite of the small deviation of the zero y-axis intercept, the linearly of the plot I_p as function of $v^{1/2}$ can be considered as a kinetic parameter, also confirming the quasi-reversible electron transfer kinetic for all the 3D electrodes. Furthermore, it is also observed that the highest I_p values for the 3D/Ti-BDD electrode (at low scan rates) compared to those for 3D/Ti-NCD and for 3D/Ti-RVC electrodes. Two reasons may be attributed for these high I_p values, (i) increase of the high electrical conductivity due the boron doping presented in this film, which is responsible to the increase of crystallographic defects and (ii) a more active surface for electron transfer reaction, due to the smaller amount of sp^2 carbon impurities which contribute to the presence of a low amount of oxygen terminated in the BDD surface.

The third aspect to be considered with respect to the electrode kinetic is the surface roughness. According to SEM results showed in Sects. Diamond films on 3D porous ti as a function of the Argon concentration and One-step HFCVD-diamond coating process using a solid carbon source, it is observed that the surface of 3D/Ti-NCD and of 3D/Ti-RVC electrodes are characterized by a drastic reduction of the grain sizes. This decrease of the grain size, consequently, decreases the surface roughness of 3D/Ti-NCD and of 3D/Ti-RVC electrodes. In this way, the surface of the 3D/Ti-BDD is rougher than that for the others two electrodes here considered. Such condition also reveals more rapid electron transfer kinetic for the 3D/Ti-BDD electrode. Similar results were shown by Pleskov et al. [44] that evaluated the electrochemical response of different BDD electrodes deposited on the Ti substrate and submitted to different treatment to obtain the different roughness level. It was observed that electron transfer reactions are faster for the electrodes with greater surface roughness.

Taking into account the kinetics parameters evaluated for the $Fe(CN)_6^{4-/3-}$ redox couple, a strong influence of the surface conditions, associated to sp^2 carbon impurities amounts, active surface, and surface roughness were verified in the electron transfer kinetic on these electrodes. The 3D/Ti-BDD, the 3D/Ti-NCD, and the 3D/Ti-RVC electrodes showed a quasi-reversible behavior. However, the 3D/Ti-BDD electrode presented fastest electron transfer kinetic. The quasi-reversible behavior of redox reactions investigated with these electrodes may be associated with the low electron transfer kinetic on these electrodes are insufficient to keep the equilibrium of species in the solution interface.

Conclusion

Sintered compacts of pure titanium containing internal or 3D porosity may be used as a substrate for the deposition of micro and nanocrystalline diamond by HFCVD technique. Among the relevant aspects, we highlight the role of powder metallurgy. P/M showed to be a powerful tool for obtaining Ti compact with controlled porosity. Therefore, adjustment of processing parameters allows obtaining sintered compacts of Ti with open and interconnected pores able to allow infiltration of reactive gases during the deposition process of diamond and also obtain 3D composites of diamond supported by a porous matrix with mechanical properties compatible with those of materials currently used for the production of electrodes.

With regarded to the deposition parameters of diamond films by HFCVD technique. The deposition temperature is shown to be a critical parameter, since it contributed significantly to the evolution of the interlayer formed between the diamond film and titanium substrate, the formation of hydride and carbide phase. The study of deposition parameters shows that in addition to work in low temperature deposition is important to choose parameters that provide a high rate of nucleation of CVD-diamond in the early stages of growth as a way to accelerate the TiC layer growth process, which may contribute to reduce the rate of diffusion of hydrogen in titanium matrix.

On the way to the route for the deposition of diamond on substrates containing 3D porosity, some aspects should be considered when choosing the parameters for the deposition of diamond film. This choice should focus on parameters that insure the coating of substrates in their most internal pores, where the entrance of radical precursors and growth is underprivileged. It is also important to choose the parameters that minimize the process of hydrogenation of the substrate.

The combined use of SEM, Raman spectroscopy, XRD, and GIXRD techniques allows the understanding the diamond growth sequence on those substrates. This sequence is understood starting from the substrate through the interface and reaching the diamond film as summarized in the following explanation. At the beginning of the diamond deposition hydrogen quickly spread in Ti matrix. The carbon in the gaseous atmosphere during growth also reacts with the matrix of Ti to form the titanium carbides. As the deposition temperature is increased the amount of formed TiC increases. Then, a competition process is established between the formation of this phase by the reaction of carbon with titanium and diamond nucleation. This competition with the chemical attack of hydrogen is crucial in the deposition process. As the TiC phase intensities increase with the temperature, the morphology of deposited diamond surface develops into a morphology formed by clusters of nanograins. In this way, the latter morphology may be related to the precipitation of TiC phases. However, factors such as surface reconstruction at high temperatures and also the low ratio of H/C should be considered. The low H/C ratio directly influences the reduction of grain size favoring the formation of nanodiamond, which enables the observation of changes in these deposition mechanisms from micro to nanodiamond. The structure of interfacial layer during the diamond growth evolves through a gradual transition from a mixture of phases formed by the sequence: titanium hydride (with preferred orientation $\langle 111 \rangle$), hydride + carbide ($\langle 111 \rangle$ and $\langle 200 \rangle$) titanium, titanium carbide ($\langle 111 \rangle$ and $\langle 200 \rangle$) and finally, diamond preferentially oriented in the direction $\langle 111 \rangle$.

In summary, the electrodes 3D-Ti/BDD, 3D-Ti/NCD, and 3D-Ti/RVC appeared consistent in their electrochemical properties with those of diamond films deposited on silicon substrates. So, they are very promising to use as electrodic materials.

Acknowledgements The authors would like to thank FAPESP, CNPq, and CAPES for the financial support. Especially thanks are given to Prof. Dr. Cairo CAA, from AMR/CTA, by providing the facilities to produce the porous titanium samples and to Dr. Matsushima JT, from LAS/INPE by the discussions concerning the electrochemical results.

References

1. Froes FH, Eylon D, Friedman G (2000) In: ASM International titanium P/M technology, vol. 7, 2nd edn. ASM Handbook, Materials Park, OH, p 748
2. Weis RS, Bania PJ, Eylon D, Semiatin SL (1996) Advances in the science and technology of titanium alloy processing. TMS, Warrendale
3. Bradbury S (1979) Source book on powder metallurgy. American Society for Metals, Metals Park, OH
4. Klar E (1983) Powder metallurgy: applications, advantages and limitations. American Society for Metals, Metals Park, OH
5. Eylon D, Field M, Froes FH, Eichelman GE (1981) Soc Adv Mater Proc Equip Quart 12:19
6. Froes FH, Eylon D, Friedman, G (2000) In: ASM international (ed) titanium P/M technology. 7:164-168, 2nd edn. ASM Handbook, Materials Park, OH

7. Krone L, Schuller E, Bram M, Hamed O, Buchkremer HP, Stover D (2004) Mater Sci Eng A 378:185
8. Bewlay BP, Gigliotti MFX, Hardwicke CU, Kaibyshev OA, Utyashev FZ, Salischev GA (2003) J Mater Proc Technol 135:324
9. Hu ZM, Dean TA (2001) J Mater Proc Technol 111:10
10. Yamamoto T, Otsuki A, Ishihara K (1997) Mater Sci Eng A 240:647
11. Green SM, Grant DM, Kelly NR (1997) Powder Metall 40:43
12. Pierson HO (1993) Handbook of carbon, graphite, diamond and fullerenes: properties, processing and applications. Noyes Publication, Park Ridge
13. Salgueiredo E, Almeida FA, Amaral M, Fernandes AJS, Costa FM, Silva RF, Oliveira FJ (2009) Diamond Relat Mater 18:264
14. Lim PY, Lin FY, Shih HC, Ralchenko VG, Varnin VP, Pleskov YuV, Hsu SF, Chou SS, Hsu PL (2008) Thin Solid Films 516:6125
15. Askari SJ, Chen GC, Lu FX (2008) Mater Res Bull 43:1086
16. Askari SJ, Chen GC, Akhtar F, Lu FX (2008) Diamond Relat Mater 17:294
17. Gerger I, Haubner R (2008) Int J Refract Met Hard Mater 26:438
18. Askari SJ, Akhtar F, Chen GC, He Q, Wang FY, Meng XM, Lu FX (2007) Mater Lett 61:2139
19. Jozwik K, Karczemska A (2007) Diamond Relat Mater 16:1004
20. Kulesza S, Patyk JK, Daenen M, William OA, Van De Putte W, Fransaer J, Haenen K, Nesladek M (2006) Surface Coat Techn 201:203
21. Okroj W, Kaminska M, Klimek L, Szymanski W, Walkowiak B (2006) Diamond Relat Mater 15:1535
22. PLeskov YV, Evstefeev AYE, Krotova MD, Lim PY, Chu SS, Ralchenko VG, Vlasov II, Kononenko VV, Varnin VP, Teremetskaya IG, Shi HC (2005) Rus J Electrochem 41:337
23. Chen X, Chen G (2004) J Electrochem Soc 151:B214
24. Gerger I, Haubner R, Kronberger H, Fafilek G (2004) Diamond Relat Mater 13:1062
25. Narayan RJ (2004) J Adhes Sci Technol 18:1339
26. Hian LC, Grehan KJ, Goeting CH, Compton RG, Foord JS, Marken F (2003) Electroanalysis 15:169
27. Vandenbulcke MC, Sainte Catherine MC (2003) Wear 255:1022
28. De Barros MI, Vandenbulcke L, Chinsky L, Rats D, Von Stebut J (2001) Diamond Relat Mater 10:337
29. Carlsson JO, Martin PM (2010) Handbook of deposition technologies for films and coatings. Science, applications and technology. William Andrew Publishing, Noyes
30. Salgueiredo E, Amaral M, Neto MA, Fernandes AJS, Oliveira FJ, Silva RF (2011) Vacuum 85:701
31. Ali Erdemir, Andrey A. Voevodin (2010) In: Martin PM (ed) Handbook of deposition technologies for films and coatings, 30 edn, Chap 14. Elsevier, Amsterdam, p 679
32. Fortunato W, Chiquito AJ, Galzerani JC, Moro JR (2007) J Mater Sci 42:7331. doi:10.1007/s10853-007-1575-0
33. Szweda R (2006) III-Vs Rev 19:40
34. Anders A (2005) Surface Coat Technol 200:1893
35. Sung-Soo Lee, Takai O, Itoh H (1997) J Mater Sci 32:2417. doi:10.1023/A:1018513425533
36. May PW, Mankelevich Yu A (2007) J Appl Phys 101:1
37. May PW, Mankelevich YA (2006) Mat Res Symp Proc PV-956, 0956-J07-04 (part of the Proceedings of Symposium J of the Fall 2006 MRS meeting)
38. May PW, Mankelevich YA (2006) J Appl Phys 100:1
39. May PW, Harvey JN, Smith JA, Mankelevich Yu A (2006) J Appl Phys 99:1
40. Polfer NC, Oomen J, Pirali O, Ueno Y, Maboudian R, May PW, Filik J, Dahl JE, Liu S, Carlson RMK (2006) J Mol Spectrosc 238:158
41. Arsene S, Bai JB, Bompard P (2003) Metall Mater Trans A 34:553
42. Guillot I, Feaugas X, Clavel M (2001) Scr Mater 44:1011
43. Buccioni E, Braca E, Kenny JM, Terranova ML (1999) Diamond Relat Mater 8:17
44. Pleskov YV, Evstefeeva YE, Krotova MD, Lim PY, Shih HC, Varnin VP, Teremetskaya IG, Vlasov II, Ralchenko VG (2005) J Appl Electrochem 35:857
45. Azevedo AF, Corat EJ, Ferreira NG, Trava-Airoldi VJ (2005) Surface Coat Technol 194:271
46. Azevedo AF, Corat EJ, Leite NF, Trava-Airoldi VJ (2002) Diamond Relat Mater 11:550
47. Azevedo AF (2003) Estudos de aderência e tensões intrínsecas e extrínsecas entre filmes finos de diamante-CVD de alta pureza e de alta taxa de nucleação e Ti6Al4 V. Doctor thesis, Faculdade de Engenharia Química de Lorena (ed), Lorena
48. Diniz AV (2002) Estudos para a obtenção de eletrodos a partir de filmes finos de diamante CVD dopados com boro em grandes áreas e aplicações em sistemas de limpeza de água, Master lecture. Instituto Tecnológico de Aeronáutica, São José dos Campos
49. Fu Y, Loh NL, Yan B, Sun CQ, Hing P (2000) Thin Solid Films 359:215
50. De Barros MI, Rat D, Vandenbulcke L, Farges G (1999) Diamond Relat Mater 8:1022
51. Feng XU, Dun-wen ZUO, Wen-zhuang LU, Yong-wei ZHU, Min WANG (2009) Trans Nonferr Metal Soc China 19:s722
52. Ižák T, Marton M, Varga M, Vojs M, Veselý M, Redhammer R, Michalka M (2003) Vacuum 84:49
53. Lee WS, Yu J, Lee TY (2005) J Mater Sci 40:5549. doi:10.1007/s10855-005-4548-y
54. Long-bin L, Xiao-jun H, He-sheng S, Xian-chang H (2004) J Mater Sci 39:1135. doi:10.1023/B:JMSC.0000012963.04082.a1
55. Khang M, Xia Y, Wang L, Gu B (2005) J Mater Sci 40:5269. doi:10.1007/s10853-005-0737-1
56. Ramesha R (1999) J Mater Sci 34:1439. doi:10.1023/A:1004590029830
57. Colley AL, Williams CG, Johansson UD, Newton ME, Unwin PR, Wilson NR, Macpherson JV (2006) Anal Chem 78:2539
58. Pleskov YV (2006) Prot Metals 42:103
59. Suffredini HB, Salazar-Banda GR, Tanimoto ST, Calegaro ML, Machado SAS, Avaca LA (2006) J Brazilian Chem Soc 17:257
60. Xie ST, Shafer G, Wilson CG, Martin HB (2006) Diamond Relat Mater 15:225
61. Balducci A, D'amico A, Di Natale C, Marinelli M, Milani E, Morgada ME, Pucella G, Rodriguez G, Tucciarone A, Verona-Rinati G (2005) Sensor Actuators B Chem 111–112:102
62. Bennett JA, Wang J, Show Y, Swain M (2004) J Electrochem Soc 151:E306
63. Gerger I, Haubner R (2007) Diamond Relat Mater 16:899
64. Braga NA, Cairo CAA, Ferreira NG (2007) Quimica Nova 30:450
65. Braga NA, Piorino Neto F, Baldan MR, Cairo CAA, Ferreira NG (2008) Mater Sci Forum 591593:289
66. Chen CQ, Li SX, Zheng H, Wang LB, Lu K (2004) Acta Mater 52:3697
67. Davis R (1993) Diamond films and coatings: development, properties and applications. Noyes Publications, New Jersey
68. Fan QH, Pereira E, Grácio J (1999) J Mater Sci 34:1353. doi:10.1023/A:1004566502572
69. Gupta S, Morell G, Katiyar SG, Gilbert DR, Singh RK (2000) J Mater Sci 35:6245. doi:10.1023/A:1026753916705
70. Guo L, Chen G (2007) Diamond Relat Mater 16:1530
71. Bühlmann S, Blank E, Haubner R, Lux B (1999) Diamond Relat Mater 8:194

72. Kim JW, Baik YJ, Eun KY (1991) Applications of diamond films and related materials. Elsevier, Amsterdam
73. Singh J, Vellaikal M, Dat R (1994) Thin Solid Films 238:133
74. Haubner R, Lux B (2002) Int J Refract Metals Hard Mater 20:93
75. Schäfer L, Klages CP, Méier U, Kohse Höinghaus K (1991) Appl Phys Lett 58:571
76. Cappuccio G, Sessa V, Terranova ML (1996) Appl Phys Lett 69:4176
77. Bruno P, Bénédic F, Mohasseb F, Silva F, Hassouni K (2005) Thin Solid Films 482:50
78. Thing JM, Shih W (2001) Mater Chem Phys 72:185
79. Chu PK, Li L (2006) Mater Chem Phys 96:253
80. Woehrl N, Buck V (2007) Diamond Relat Mater 16:748
81. Cicala G, Bruno P, Bénédic F, Silva F, Hassouni K, Senesi GS (2005) Diamond Relat Mater 14:421
82. Terranova ML, Rossi M, Vitali G (1996) J Appl Phys 80:3552
83. Yang TS, Lai JY, Cheng CL, Wong MS (2001) Diamond Relat Mat 10:2161
84. Rabeau JR, John P, Wilson JIB, Fan Y (2004) J Appl Phys 96:6724
85. Birrell J, Gerbi JE, Auciello O, Gibson JM, Johnson J, Carlisle JA (2005) Diamond Relat Mat 14:86
86. Silva F, Bénédic F, Bruno P, Gicquel A (2005) Diamond Relat Mat 14:398
87. Partridge PG, Ashfold MNR, May PW, Nicholson ED (1995) J Mater Sci 30:3973. doi:10.1007/BF00360696
88. Miranda CRB, Azevedo AF, Baldan MR, Beloto AF, Ferreira NG (2009) J Nanosc Nanotech 9:3877
89. Silva WM, Ferreira NG, Travello J, Almeida EC, Azevedo AF, Baldan MR (2007) Diamond Relat Mater 16:1705
90. Glaser A, Rosiwal SM, Freels B, Singer RF (2004) Diamond Relat Mater 13:834
91. Glaser A, Rosiwal SM, Singer RF (2006) Diamond Relat Mater 15:49
92. Baldan MR, Almeida EC, Azevedo AF, Ferreira NG (2007) Appl Surf Sci 254:600
93. Baldan MR, Ramos SC, Almeida EC, Azevedo AF, Ferreira NG (2008) Diamond Relat Mater 17:1110
94. Gonçalves ES, Rezende MC, Ferreira NG (2006) Brazilian J Phys 36:264
95. Weimer WA, Cério FM, Johnson CE (1991) J Mat Res 6:2134
96. Baldan MR, Ramos SC, Almeida EC, Azevedo AF, Ferreira NG (2008) Diam Relat Mat 17:1110
97. Martin HB, Argoitia A, Landau U, Anderson AB, Angus JC (1996) J Electrochem Soc 143:L133
98. Granger MC, Xu JS, Strojek JW, Swain JM (1999) Anal Chim Acta 397:145
99. Show Y, Witek MA, Sonthalia P, Swain GM (2003) Chem Mater 15:879
100. Panizza M, Cerisola G (2005) Electrochim Acta 51:191
101. Foti G, Gandini D, Comninellis C, Perret A, Haenni W (1999) Electrochem Solid State Lett 2:228
102. Granger MC, Swain GM J (1999) J Electrochem Soc 146:4551
103. Greef R, Peat R, Peter LM, Pletcher D, Robinson J (1985) In: Instrumental methods in electrochemistry. John Wiley & Sons, New York
104. Chen P, McCreey RL (1996) Anal Chem 68:3958
105. Tryk DA, Tsunozaki K, Rao TN, Fujishima A (2001) Diam Relat Mater 10:1804